Metallurgical and Materials Transactions A manuscript No.
(will be inserted by the editor)

Continuous grain size gradients in austenitic Incoloy 800H: design, processing and characterization

Catherine M. Bishop · Shaun P. Mucalo · Milo V. Kral · Daniel J. Lewis

December 5, 2019

Abstract Grain size variations are common in thermo-mechanically processed alloys with non-uniform cold work. A method to produce samples with grain size gradients was developed using Incoloy 800H. Two tensile samples with non-uniform gages were designed with finite element analysis and manufactured. Measured strain profiles were consistent with designs, and maximum von Mises strains of $(18.6 \pm 6.1)\,\%$ and $(13.6 \pm 4.6)\,\%$ were obtained. After annealing, an area $40\,\text{mm} \times 5\,\text{mm}$ was mapped by electron backscatter diffraction. Totals of 2849 and 2569 grains were identified after merging twins. Both samples had duplex grain structures as defined in ASTM E1181. Grains were binned into 4 mm strips to evaluate the spatial grain size distribution. Grain size gradients of $0.0081\,\text{mm}^2/\text{mm}$ and $0.0112\,\text{mm}^2/\text{mm}$ were obtained. Simulated grain growth of the linear gradient microstructure was consistent with accelerated growth predictions. This new method of making samples will enable laboratory studies of gradient grain size effects in realistic industrial alloy microstructures. Further, samples could be used for parallel, single specimen experiments on phenomena that depend on grain size such as complexion transitions and fatigue. Most importantly, high-throughput parallel testing of microstructures enabled by our method could accelerate materials discovery and qualification in fields such as high entropy and nuclear alloys.

Research funded by Methanex New Zealand Ltd.

Corresponding author email: catherine.bishop@canterbury.ac.nz

C. M. Bishop, S. P. Mucalo, M. V. Kral

Department of Mechanical Engineering, University of Canterbury, Christchurch, 8140, New Zealand

D. J. Lewis

Department of Materials Science and Engineering, Rensselaer Polytechnic Institute, Troy NY 12180, USA

Keywords Thermo-mechanical processing · grain size gradient · heterogeneous microstructures · alloys

1 Introduction

The effect of microstructure on material performance is fundamental to materials engineering [1]. Tailoring microstructures in order to optimize properties includes creating spatially varying microstructures for optimum performance under applied fields such as stress [2], temperature [3,4] and electromagnetic fields [5,6]. Case hardening mild steel is a classic example [7]. Lee [8] used torsional deformation and annealing to obtain grain size gradients in AISI 1018 steel with improved tensile properties compared to a homogeneous grain sized alloy. Hwang [9,10] used oxide grain refiners and powder methods to obtain grain size gradients in nickel with improved fatigue resistance. Yan [11] used surface rotational rolling to obtain grain size and texture gradients in AZ31 magnesium alloy with concurrent improvements in strength and ductility. Long [12] used cryogenic surface mechanical grinding to obtain nanograined surface regions for improved fatigue performance in pure copper. Cheng [13] used direct current electrodeposition to obtain gradient nano-twinned Cu structures with both high strength and high work hardening properties.

Spatially varying microstructures can also be by-products of traditional manufacturing routes. One such example is the processing of steam reformer pigtail tubes that require 90° bends to enable the component to accomodate thermal expansion [14]. The bends are formed by rotary drawing Incoloy 800H, a high nickel austenitic steel. The plastic strain from the bending operation varies across the tube cross section, with outer fibre strain estimated to be $\approx 10\,\%$ [15] at the intrados (inner bend radius) and extrados (outer bend radius) and minimal stored plastic work at the neutral bending plane. After a recrystallization anneal, the details of which are proprietary, the grain size is non-uniform with larger grains near the neutral plane and smaller grains near the intrados and extrados, Fig. 1. Pigtails operate at elevated temperatures around 800 °C to 900 °C and internal pressures approximately 1.9 MPa such that the dominant deformation mechanism is creep [16]. Anecdotally, longitudinal creep cracks have been observed in the transition region between the large grained and the small grained zones, but there has been no systematic study of the effect of grain size gradients on creep. Understanding the relation between spatially varying grain size and creep behavior was the primary motivation for this study.

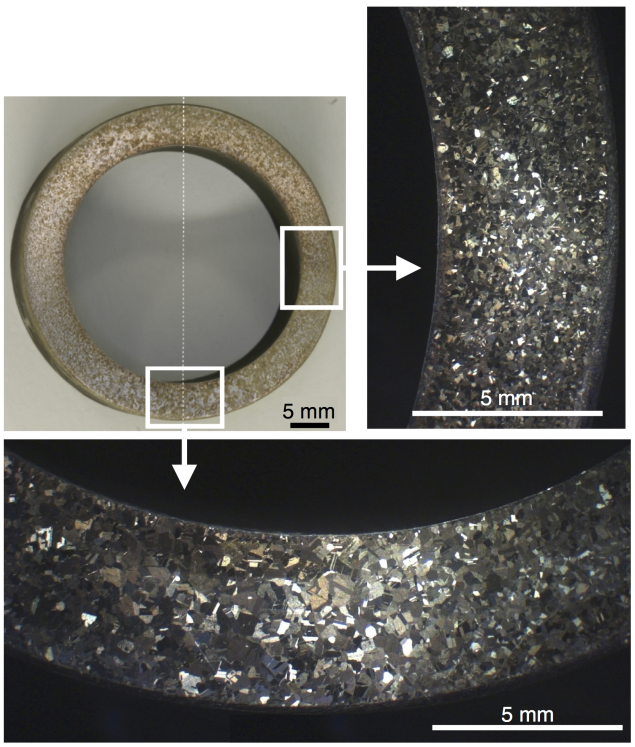

Fig. 1: Macrostructure of cross-section of 800H pigtail at bend with neutral plane indicated by vertical, white dashed line. Insets showing (below) large grains at bottom of section near the neutral plane and (right) small grains near region of maximum stored work.

Heat treatment is a common method of increasing mean grain size and can be used to manipulate spatially varying grain size distribution. A recent computational study of isotropic grain growth on a 2D domain employed gradient grain size microstructures [17]. Grain growth was simulated by motion by mean curvature in Surface Evolver [18], and, as expected, parabolic kinetics were obtained. In contrast, the parabolic grain growth constant was found to depend on the variance of the grain size distribution, a result not predicted by any current grain growth theory. The variance was obtained by introducing a linear variation in the local mean grain size as a function of distance across the domain while keeping the global mean grain size constant. A second motivation for this study was to obtain real microstuctures with controlled gradients in grain size to test Baskaran's [17] predictions.

The ASTM standards for quantifying grain size focus on measures of mean grain size (typically called grain size) [19–21] or of the largest grain in a sample [22] using optical and electron backscatter diffraction (EBSD) methods. ASTM E1181:Standard Test Methods for Characterizing Duplex Grain Sizes provides methods for determining grain size in samples with grain size distributions that deviate from single,

log-normal distributions [23]. It defines materials with topological, duplex grain sizes as "specimens or products containing grains of two or more significantly different sizes, but distributed in topologically varying patterns..." This significant difference is defined to be a difference in the ASTM grain size number (n) of 3 or more. Further, the standard gives these examples "systematic variation of grain size across the section of a product, necklace structures, banded structures, and germinative grain growth in selected areas of critical strain." For samples with topological–cross section duplex grain sizes, the Standard says to report the mean grain sizes at the extremes of the variation pattern along with an indication of the location of the extremes in the sample, e.g. at center or at surface. The spatial variation of grain size and grain size distribution are missing in this description.

Grain size gradients are produced and characterized in Incoloy 800H (UNS N08810) in this work. The alloy is an austenitic Fe-based superalloy with composition 30.0-35.0 Ni, 19.0-23.0 Cr, minimum 35.9 Fe, 0.05-0.1 C, 0.16-0.60 Al, 0.16-0.60 Ti with 0.30-1.20 (Al+Ti) and is required to have ASTM grain size $n = 5$ or coarser [24]. It was developed from Incoloy 800 and designed to have improved creep performance with higher carbon concentration and a grain size requirement compared to Incoloy 800. It is widely used at elevated temperatures in oxidizing environments. For example, it has been shortlisted for Generation IV super-critical water cooled nuclear power systems [25]. More particularly, it is used in the outlet pigtail piping of methanol reformer systems [26].

Research on Incoloy 800H has focused on grain boundary engineering and precipitation [27,28], microstructural evolution during dynamic recrystallization [29–31], properties of welds [32] and recently the creep rate equations and deformation mechanism map [33]. There is little published on static recrystallization. The manufacturer's technical report contains recommendations in graphical form for thermomechanical processing [24]. Beardsley *et al.* [34] studied recrystallization of 800H pipe after cold pilgering and found that grain growth stagnated at a limiting grain size determined by the annealing temperature. Cao *et al.* [35] studied microstructural evolution after solution annealing following hot rolling. They found that banded, recrystallized microstructures resulted for solution anneals at 950 °C and 1050 °C, but not at 1150 °C. Both authors attributed their observations to precipitation during annealing.

In this paper, a thermo-mechanical method to obtain gradient grain size samples is demonstrated using Incoloy 800H. Finite element analysis (FEA) was used to design dog bone shaped samples with non-uniform widths that were strained in a tensometer to obtain non-uniform plastic strain. Two samples with strain profiles analogous to profiles obtained in pigtails after bending were demonstrated. The recrystallized gradient grain size distributions were analyzed and metrics for them were proposed. Production of gradient grain size samples in the laboratory will enable systematic study of the the effect of these non-uniform microstructures on microstructural evolution, properties and performance. The opportunities to use this method to enable high-throughput testing are discussed.

2 Experimental Details

2.1 Sample Design

The motivation to examine gradient grain size samples was the microstructure obtained across the cross-section of the bends in reformer pigtail pipes. Two samples were designed to mimic a simplified description of the variation in stored cold work after bending a tube. Consider a thin-walled tube with Cartesian coordinates defined with the origin at the center of the tube cross-section, z-axis parallel to the axis of the tube and the cross-section parallel to the $x-y$-plane. The isotropic, linear, plastic material experiences a bending moment M_x that produces a linear variation in stress σ_{zz} as a function of distance y from the neutral $x-z$ plane at the center of the tube. This gives a linear variation in plastic strain ϵ_{zz} as a function of y and a sinusoidal variation in ϵ_{zz} with distance around the circumference of the tube. We take these linear and sinusoidal variations in stored plastic strain to represent the variation in stored plastic work in a pigtail during processing.

Linear and sinusoidal variations in plastic work were obtained in tensile samples with non-uniform gage cross sections. The dimensions are specified by the depth h and the width of the section $w(x)$, where x is the distance along the gage. A set of six tensile tests revealed that 800H had bi-linear elastoplastic behavior with elastic modulus $E = 195.5\,\text{GPa}$, yield strength $\sigma_y = 250\,\text{MPa}$ and tangent moludulus $E_T = 1.8\,\text{GPa}$. Using the small strain approximation, infinite elastic modulus and approximating the plastic von Mises strain by the axial component of strain, $\epsilon_{vm}(x) \approx \epsilon_{xx}(x)$.

$$\epsilon_{xx}(x) = \frac{1}{E_T}\left(\sigma_{xx} - \sigma_y\right) = \frac{1}{E_T}\left(\frac{F}{A(x)} - \sigma_y\right) \tag{1}$$

where σ_{xx} is the stress in the axial direction, F is the applied axial load and $A(x) = hw(x)$ is the cross-sectional area.

A cross-sectional width with form $w_l(x)$ produces a linear variation in ϵ_{xx}, and a cross-sectional width with form $w_s(x)$ produces a sinusoidal variation in ϵ_{xx}.

$$w_l(x) = \frac{B}{\left(x - \frac{L}{2}\right) + b} \tag{2}$$

$$w_s(x) = \frac{C}{\sin\left(c\left(x - \frac{L}{2}\right)\right)} \tag{3}$$

where B, C, b and c are constants and L is the total gage length.

FEA using ANSYS® Academic Research Version R15.1 was performed to tailor geometric parameters in order to obtain $\epsilon_{xx}(x = 0) = \epsilon_{max} \approx 10\,\%$ for the two profiles. The material properties are summarized in Table 1. The plane stress approximation was used to calculate the plastic strain for fixed displacement using a bilinear, isotropic hardening model. The corresponding maximum loads were determined. The linear profile was smoothed in the center to prevent stress concentrations at a sharp notch. The FEA-designed sample geometry and required tensometer parameters are given in Table 2.

2.2 Sample Treatment

Incoloy 800H 4.76 mm sheet from VDM Metals, Australia was CNC machined to manufacture two samples, hereafter referred to as linear and sinusoidal, with geometries specified in Table 2. The as-recieved mean grain size calculated from the average of 292 grains was $0.0249\,\text{mm}^2$ equivalent to $n = 2.4$. A $1\,\text{mm} \times 1\,\text{mm}$ grid was laser etched onto one surface of the gage of each sample. The samples were strained in an MTS810 tensometer to the designed maximum cross head displacements. The experimental loads required to obtain the design cross-head displacements were 25.2 kN and 22.1 kN for the linear and sinusoidal samples, respectively. These are within 4 % and 7 % of the design values. Images of the

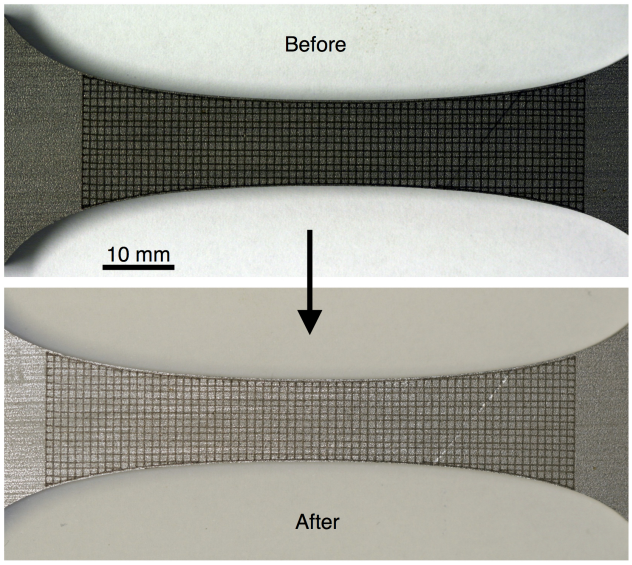

Fig. 2: Sinusoidal specimen with laser etched grid before and after extension in the tensometer. The intersections of the grid lines were used to determine plastic strain in the gage.

grids were collected before and after straining using a Canon EOS30D DSLR camera with 100 mm lens, as shown in Fig. 2.

The strain at the surface of the specimens was determined from the nodal positions of the grid before, (X, Y), and after, (x, y), extension. Optical images were processed in ImageJ [36], and the grid intersections were manually determined from the skeletonized images. The measurement error was estimated to be $\Delta = 0.05\,\mathrm{mm}$, half the width of the etched grid lines. The strain, ϵ, was determined from the deformation gradient tensor, $\mathbf{F}$, and the identity matrix, $\mathbf{I}$, using finite differences on the point cloud of nodes with

$$\mathbf{F} = \begin{bmatrix} \frac{\partial x}{\partial X} & \frac{\partial x}{\partial Y} \\ \frac{\partial y}{\partial X} & \frac{\partial y}{\partial Y} \end{bmatrix} \tag{4}$$

$$\epsilon = (\mathbf{F}^{\mathbf{T}} + \mathbf{F}) - \mathbf{I} \tag{5}$$

The deformed samples were annealed for 60 min at 1100 °C and air cooled. The recrystallized samples were prepared for metallography by sequential polishing with 180, 240, 360, 400 and 600 grit SiC paper followed by 9, 3 and 1 µm diamond paste. The final polish used 0.06 µm colloidal silica. A total area of 40 mm × 5 mm was mapped with EBSD in a JEOL 6100 scanning electron microscope with Oxford

Instruments AZtec software. Approximately 200 individual maps, each 1.2 mm × 1.05 mm, were collected with a 4 µm step size and ≈ 2 µm spot size. EBSD data analysis was performed with MTEX Toolbox in MATLAB®(2015a) [37]. Indexing rates exceeded 90 %. The orientation of unindexed points was filled by the nearest neighbor method in MTEX before the individual maps (tiles) were stitched together. An orientation tolerance of 10° for a single crystallite was used in this work. When the typical tolerance of 5° [21] for a single crystallite was used, the mosaic nature of the data set was apparent and spurious grain boundaries were identified at EBSD map intersections. An orientation tolerance of 10° yielded microstructures in the center of tiles that appeared identical on visual inspection to the 5° tolerance microstructures and removed grain boundary identification errors associated with the mosaic effect.

3 Results and Discussion

3.1 Experimental

The experimentally determined plastic strain map and strain profiles along the centerline of the gage at $y = 0$ were compared to the FEA predictions for the two samples, Fig. 3. In the following, the y-coordinate measures distance across the gage width, and the x-coordinate measures distance along the gage length with the origin at the geometric center of the sample. In both samples, ϵ_{vm}, varied along the gage length and was approximately constant across the gage width, Fig. 3 a) and d). There was some variation across the width around $x = 0$ for the sinusoidal sample, Fig. 3 d). The origin of this is not known, but subsequent analysis uses only the central 5 mm wide portion where the von Mises strain is uniform in y.

A comparison of the FEA prediction (blue line) and the measured ϵ_{vm} (circles) is favorable, Fig. 3b) and d). In each case, the FEA predictions are below the measured values but are generally within the error bars. The error bars correspond to propagation of measurement error from the location of the nodes and were significant. The stored work in the linear sample showed an increasing trend over $-22\,\text{mm} < x < -4\,\text{mm}$ and flattened out before decreasing again from approximately $x = 4$ mm, Fig. 3b). The maximum measured strain in the central flat of the gage was higher than the FEA predicted maximum strain $\epsilon_{vm} = (18.6 \pm 6.1)\,\% > 11.6\,\%$. However, the mean value over the 8 mm flat section

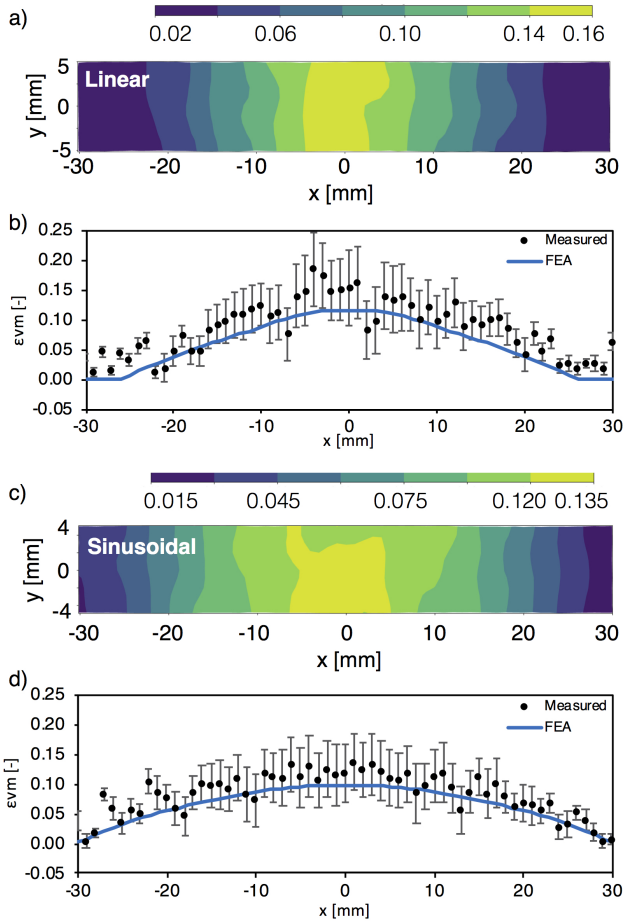

Fig. 3: Contour plots of experimentally determined von Mises plastic strain over a rectangular region in the center of the gage for a) the linear and c) the sinusoidal sample. The corresponding color bars use the same relative scale. Comparison of experimental and finite element (FEA) predicted von Mises strain along the gage centerline at $y = 0$ for b) the linear and d) the sinusoidal samples. Error bars correspond to propagated measurement error.

was $(14.4 \pm 6.6)\,\%$, which compares favorably with the prediction in the linear sample. The stored work in the sinusoidal sample had a smooth variation with distance along the gage, as designed, and lower absolute values compared to the linear sample, Fig. 3d). The maximum measured strain of $(13.6 \pm 4.6)\,\%$ compares favorably with the FEA predicted maximum $9.8\,\%$. Overall, spatially varying plastic stored work was obtained in the two samples with a discernible difference in the shapes of the spatial variations.

After annealing the samples in air, EBSD mapping was performed on approximately one half of the total gage length of each sample. The inverse pole figure (IPF) colored raw map, grain boundary character map and grain size colored map for each sample are presented in Fig. 4. The IPF maps illustrate that

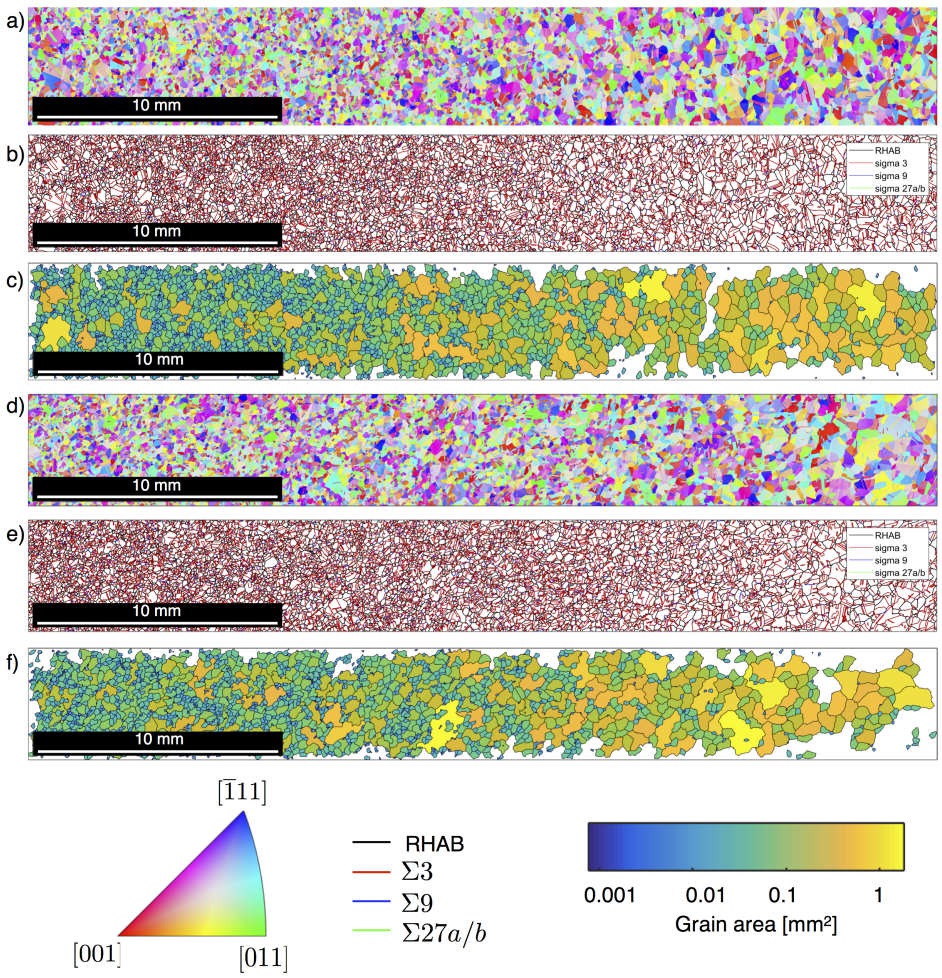

Fig. 4: Microstructural mapping from EBSD data from approximately half of the gage length of each sample. The left of the images corresponds to the center of the gage that experienced the maximum strain, and the right of the images corresponds to the region near the grips that obtained minimum plastic strain. Orientation maps are shown in a) and d), grain boundary character maps in b) and e) and grain size maps in c) and f) for the linear and sinusoidal samples, respectively.

177 there was no preferred texture development in either sample. This is consistent with Cao *et al.*'s analysis
178 of hot rolled 800H annealed at 950 °C [35].

179 The grain boundary character was categorized into random high angle boundary (RHAB), $\Sigma 3$, $\Sigma 9$ or $\Sigma 27$,
180 Fig. 4 b) and e), where the Palumbo and Aust criterion was applied for the special boundaries[38]. Grain
181 boundaries with misorientation $> 10°$ were identified as RHAB. The length fraction of $\Sigma 3$ boundaries
182 in the as-received plate was 46 % and increased to 53 % in both the linear and sinusoidal samples. The
183 length fraction of $\Sigma 9$ boundaries increased from 2 % in the as-received to 4 % in both samples. While

length fractions of special boundaries can be increased by sequential thermomechanical processing (grain boundary engineering) to upwards of 70 % in low stacking fault alloys, only a minor increase occurred here [39].

When twin-related volumes were merged, the network of high angle grain boundaries spanned the analysis domain. Grains that were truncated by the edges of the map were discarded for computing statistics. These remaining twin-merged volumes will be referred to as grains in this work. The grain area colored maps, Fig. 4 c) and f) for linear and sinusoidal samples, respectively, showed a spatial variation in grain size from left to right. The smallest (blue green) grains are concentrated on the left and the largest (yellow) grains are concentrated on the right. The white areas in the plots correspond to regions with fewer than 25 pixels per grain or grains that were truncated by the edge of the image. The second type of information loss is a particular problem towards the right hand side of the images where large grains that are truncated by the edge of the map extend up to the center of the map at $y = 0$. This highlights the compromise between total mapping area and step size, where the number of large grains is traded off against the resolution of the smallest grains. While this is always a consideration for orientation mapping, it is a particular issue in these gradient microstructures.

The overall sample grain size distributions were analyzed using grain area, Fig. 5 a) and b). A total of 2849 grains with sample mean grain size $\mu = 0.0641\,\mathrm{mm}^2$ and sample variance $\sigma^2 = 0.0138\,\mathrm{mm}^4$ were identified in the linear sample. A total of 2569 grains with $\mu = 0.0688\,\mathrm{mm}^2$ and $\sigma^2 = 0.0206\,\mathrm{mm}^4$ were identified in the sinusoidal sample. The quantile-quantile plots, Fig. 5 c) and d), demonstrate that the log-normal distribution was a better fit to the data than a normal distribution for small to intermediate grain sizes. However, the log-normal distribution underestimates the actual number of small grains and overestimates the actual number of large grains in the samples. Vander Voort and Friel [40] recommended using area weighted grain area distributions to determine whether a grain size distribution is bimodal and contains a small number density of very large grains. This was the case in both samples, Fig. 5 c) and d). What is missing in the analysis to date is a method for capturing the spatial variation of the grain size distributions.

A method for analysing the spatial variation in pore size distributions from geology was adapted to visualize the spatial variation in grain size [41]. The cumulative number distribution of grains was plot-

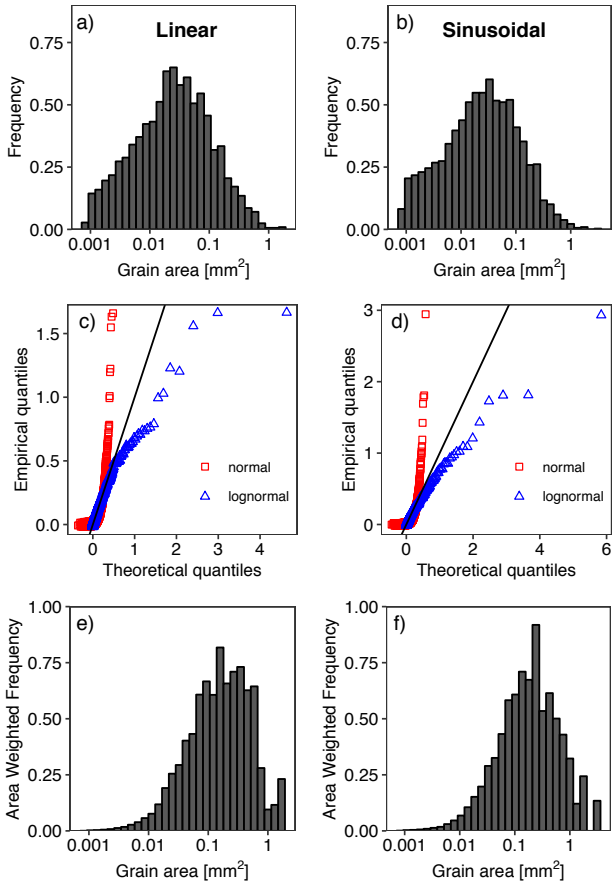

Fig. 5: Sample grain size analysis with a) and b) grain area frequency distributions, c) and d) quantile-quantile plots illustrating the deviation of grain area frequency from best fit log-normal distribution and e) and f) the area weighted grain area distributions for linear and sinusoidal samples, respectively.

ted against fractional distance along each map, X with $0 \leq X \leq 1$, Fig. 6. In alloys with grain size distributions that are spatially uniform, the data will fall about the uniform distribution (dashed line). Whereas pores do not fill space, grains do and therefore the discrete data for each sample appeared as lines. Both samples showed significant deviations from the uniform spatial distribution. Small grains were clustered near the center of the gage near $X = 0$, and large grains were clustered near the end of the gage near $X = 1$. While Fig. 6 illustrates some spatial variation, it is missing information on the grain size distributions.

Grains were binned by the location of their centroids along the gage length, and the distribution of grain areas in each bin led to the violin plots in Fig. 7. The bins are labelled with the x-coordinate of the center of the bin. Because the bin size was fixed at 4 mm, the number of grains included in each violin plot

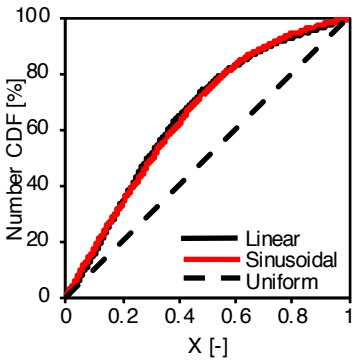

Fig. 6: Cumulative number distribution plotted against fractional distance along mapped region of the gage for the linear and sinusoidal samples compared to the spatially uniform distribution.

varied and is given above each plot. The number of grains per bin ranged from 96 to 538 in the linear sample, Fig. 7 a), and from 70 to 449 in the sinusoidal sample, Fig. 7 b). ASTM Standard E2627 [21] requires at least 500 grains to be identified by EBSD, and this was only obtained in 2 bins in the linear sample. The bin size is a compromise between being large enough to ensure a reasonable number of grains per bin and being small enough to capture the gradient in grain size and distribution with distance. One could imagine using a fixed number of grains per bin or using a fixed bin size to examine the spatial variation, but each method has drawbacks.

In both samples, the first bin centered at 2 mm had fewer grains than the next bin centered at 6 mm. There are several factors that contribute to this. One was the effect of truncation of the sample that meant that each grain that was bisected by the far left-hand boundary of Fig. 4 a) or d) was excluded from the statistics, and this was a large number because of the small grain sizes in that area. A second factor was that the smallest grains in the analysis of both samples were approximately 8×10^{-4} mm^2 due to a combination of EBSD step size of 4 µm combined with the minimum of 25 pixels per twin volume and the merging of twin related volumes to form grains.

Using the bins in Fig. 7, the moments of each distribution were calculated, Table 3 and Table 4. The zeroeth moment is the number of grains, N. The first moment is the mean grain size, μ, and the second central moment σ^2 is the variance of the distribution. The mean grain size of the small grained region was overestimated here due to undercounting of the smallest grains due to EBSD step size limitations.

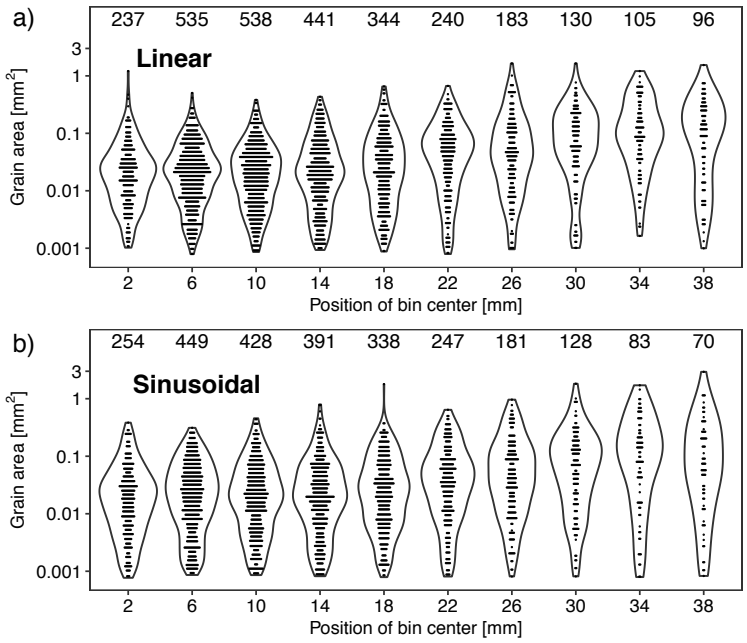

Fig. 7: Violin plots of the grain area distributions for grains sorted into 4 mm bins spaced at 4 mm intervals along the gage for a) the linear and b) the sinusoidal samples. The bins are labelled with the x-coordinate of the center of the bin. The dot density plots show the actual data points, and the number of grains in each distribution is given at the top.

In contrast, the mean grain size of the large grained region was underestimated due to the likelihood of the largest grains being bisected by the sample and excluded from the statistics.

The mean grain size with error bars corresponding to standard error of the mean was plotted with distance along the image, Fig. 8. Both samples displayed similar trends in mean grain size with fairly uniform small mean grain sizes in the bins $2\,\text{mm} < x < 14\,\text{mm}$, increasing mean grain sizes in the bins $18\,\text{mm} < x < 34\,\text{mm}$ and a plateau in mean grain size $x \geq 34\,\text{mm}$.

Systematic variations in the mean grain size with distance along the samples were achieved. The gradient in mean grain size was estimated from the bins $18\,\text{mm} < x < 34\,\text{mm}$ to be $0.0081\,\text{mm}^2/\text{mm}$ in the linear sample and $0.0112\,\text{mm}^2/\text{mm}$ in the sinusoidal sample. These estimates of grain size variation corresponded to ASTM grain size number differences $\Delta n = 1.7$ and $\Delta n = 2.1$, respectively. Neither sample as characterized here met the ASTM definition of a duplex grain structure [23]. While the number of grains in the small grained statistics was in the hundreds, the large grained regions had significantly lower than the recommended mapping of 500 grains for determining the mean grain size [21]. ASTM

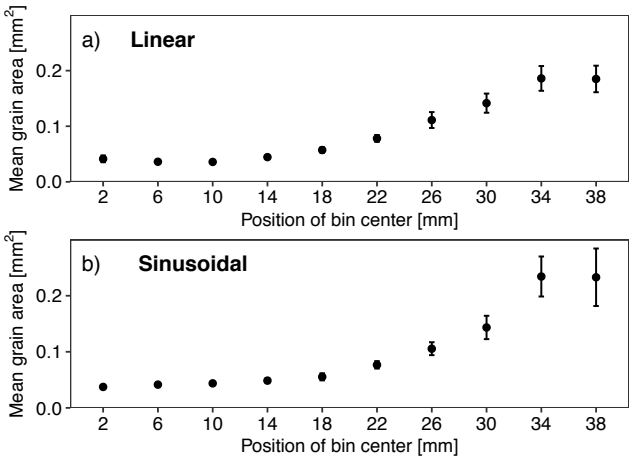

Fig. 8: Mean grain areas from distributions in Fig. 7 for a) the linear and b) the sinusoidal samples. The error bars correspond to standard error of the mean.

Standard E930 [22] provides a method for determining n of an outlier grain that can be used with ASTM Standard E1181 [23] for duplex microstructures. In the linear sample, the largest single grain (outlier grain) had area $1.6457\,\mathrm{mm}^2$ and $n = -3.5$. In the sinusoidal sample, the largest single grain had area $2.9338\,\mathrm{mm}^2$ and $n = -4$. Using these, $\Delta n > 3$ exceeded the Standard's threshold for duplex microstructure distributions in both samples.

All grains in a microstructure contribute to the grain size statistics in the analysis presented here. In contrast, in previous work where gradient grain size samples were characterized either mean grain size was determined from small regions along the direction of grain size variation [8] or topological duplex grain sizes were obtained, such as in the nanograined surface regions [11] or layered nickel alloys [9]. Continuous variation in grain size has not been characterized in the literature.

In surface treated samples, authors report nanograined surface regions and micron-sized grains in the interior: Yan [11] reported transverse grain sizes of 170 nm and 20 µm, respectively, while Long [12] reported grain sizes of 60 nm and 21 µm, respectively. In samples with grain size manipulated with oxide dispersions, Hwang [9] reported grain sizes in the finest region of 22 µm and 154 µm in the coarsest region. Lee [8] reported surface grain sizes of 8 µm and interior grains of 13.8 µm in torsionally processed samples.

A parametric plot revealed the relationship between measured stored plastic work and the post annealing grain size, Fig. 9. The data points are mean values corresponding to the 4 mm bins used previously. The

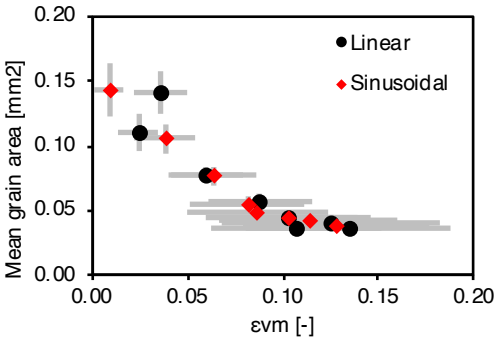

Fig. 9: Parametric plot of mean grain size with mean measured von Mises plastic strain for 4 mm bins centered at 2 mm to 30 mm along gage for the linear and the sinusoidal samples. Vertical error bars are standard error of the mean grain size, and horizontal error bars are mean von Mises plastic strain measurement error.

mean grain size has error bars for standard error of the mean for the bin. The ϵ_{vm} is the average of ϵ_{vm} over the 4 mm bin with error bars for mean measurement error. The plot includes bins in the range 2 mm to 30 mm only because the strain measurement was limited to this region. The largest ϵ_{vm} corresponded to the center of the total gage and the bin centered at 2 mm where the smallest grains were found. The smallest ϵ_{vm} corresponded to the end of the gage and the largest grains. The recrystallized grain size was a decreasing function of cold work, consistent with the theory [42]. In fact, this is the very processing-structure relationship that we set out to exploit in the sample design.

The parametric data sets for the two samples in Fig. 9 overlap suggesting that the recrystallized grain size is insensitive to the gradient in stored work at this length scale. Various methods to simulate the deformation and subsequent recrystallization at the microstructural level have been developed including integrated phase-field and crystal plasticity models that deal with nucleation by strain induced grain boundary migration mechanism [43] or by subgrain growth in the context of strain gradient theory [44]. In order to use such a method to explore the deformation and recrystallization in the samples with mesoscopic strain gradients over 35 mm, much larger, irregularly shaped simulation domains would be required. This is a significant modelling challenge.

While there was no direct evidence of the critical strain for initiation of static recrystallization for 1 hour at 1100 °C, this phenomenon was not ruled out by the results [45]. The recrystallized grain size is a decreasing function of the amount of cold work above a threshold critical strain [46]. The largest

recrystallized grains are obtained at this critical strain, and these can be as large as millimeter-sized in aluminum alloys, where the critical strain can correspond to 12 %RA [46]. No recrystallization or grain refinement, just recovery, occurs for cold worked regions with strains less than the critical value. A decrease in grain size and unrecrystallized grains at very low cold work would constitute direct evidence of the critical strain, and that was not observed here. The laser etched grid allowed strain measurement over a total 60 mm, Fig. 3, and did not include the very lowest strain regions at the far ends of the gage. Further, the smallest recrystallized grain size for any bin exceeded the grain size of the as-received material ($0.0358\,\mathrm{mm}^2 < 0.0249\,\mathrm{mm}^2$), indicating that grain growth had followed recrystallization during the heat treatment.

3.2 Stress Distribution Simulation

The primary motivation of this research was to understand the role of grain size gradients on creep performance of pigtail tubes. While a method for making gradient samples has been developed, no creep testing has yet been performed on them. As stress drives defect transport in creep [47], a preliminary finite element calculation was performed on the sinusoidal microstructure in the hopes of identifying stress concentrations linked to the gradient in crystallite size.

Finite element simulations were performed on the sinusoidal sample microstructure using OOF2 [48]. The raw EBSD mapped orientations after filling using nearest neighbors for unindexed points were used. The grain identification from the fully processed EBSD data set was used to generate the finite element mesh. The single crystal elastic constants are not known for 800H; therefore, representative values corresponding to Fe-18Cr-14Ni alloy were used with $C_{11} = 198\,\mathrm{GPa}$, $C_{12} = 125\,\mathrm{GPa}$ and $C_{44} = 122\,\mathrm{GPa}$ [49]. A plane stress simulation with $\sigma_{xx} = 2\sigma_{yy} = 9.5\,\mathrm{MPa}$ corresponding to the hoop stress in a thin-walled pressure vessel with the axial coordinate alined with y and the circumferential coordinate aligned with x in this geometry.

The von Mises stress distribution for the finite element simulation on the sinusoidal sample is shown in Fig. 10. The black lines indicate the network of RHABs. The calculations were based on local lattice orientations, and strain contrast between twin related volumes is visible in the color contrast in the large

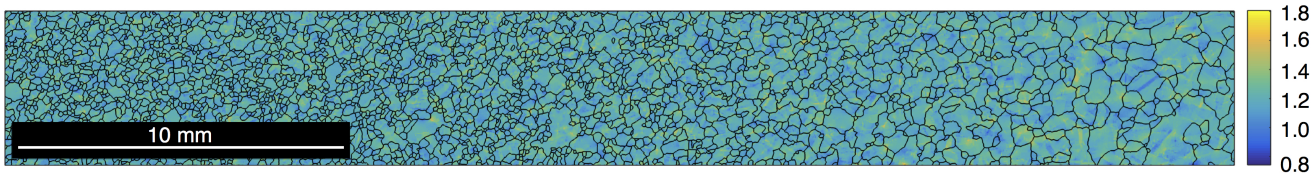

Fig. 10: Von Mises stress distribution predicted by OOF2 finite element simulation of plane stress elastic deformation of the sinusoidal sample with crystallographic orientations corresponding to Fig. 4d). Black lines show the high angle grain boundaries as in Fig. 4e). The stress scale is normalized by the hoop stress.

grains on the right side of the image. All the stresses are well below the elastic limit. Larger regions of relatively high stress, yellow, were evident in the large grained region to the right. The implications for locations of damage accumulation are not obvious at this stage. In fact, the nature of the mechanisms for creep cavitation in alloys is an open research question [50].

An integrated multi-scale model incorporating model grain geometries and orientations and crystal plasticity was recently demonstrated for creep in 316H stainless steel [51]. Applying this method to *model* gradient microstructures may shed light on the relation between grain size gradients and creep damage, see [52] for an example. A coupled experimental and computational approach using *real* gradient samples designed with the method introduced here could elucidate the origin of creep cavitation in industrial components such as pigtails. The effect of spatial grain size distributions can be studied by using real gradient samples for creep testing and the microstructures of those samples as input for corresponding simulations. Again, the size of the computational domain required to capture grain size statistics over a mesoscale gradient is a significant challenge.

3.3 Grain Growth Simulation

In light of Baskaran's study [17] that identified an increased early stage parabolic grain growth constant, k, for model microstructures, an identical calculation was run using the grain structure of the linear sample. See [17] for details of the method. Whereas Baskaran's initial microstructures contained approximately 38 000 grains on a 3×1 domain, 13 765 centroids corresponding to the twin volumes from the linear sample were used to generate grains on a 7×1 domain for the initial condition. The twin volumes

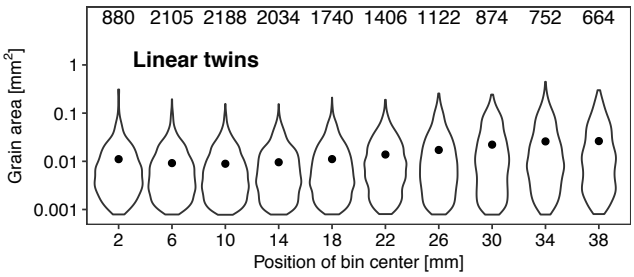

Fig. 11: Violin plots of the grain area distributions for twin volumes sorted into 4 mm bins spaced at 4 mm intervals along the gage for the linear sample. The mean and standard error of the mean are shown with a dot and whisker for each bin. The number of grains in each distribution is given at the top.

were used rather than the grains because there were so few of the latter. The corresponding statistics for the twin volumes gave a sample $\mu = 0.013\,26\,\mathrm{mm}^2$ and $\sigma^2 = 7.010 \times 10^{-4}\,\mathrm{mm}^4$. The spatial variation of grain sizes are shown in Fig. 11 and the moments of the distribution in Table 5. The twin size trends and spatial variation were consistent with the grain statistics in Fig. 7a) and Table 3.

The new simulation was terminated after 0.2 units of time with 877 grains remaining. A linear least squares fit to the sample mean grain area with time was obtained ($R^2 = 0.9998$), and the slope identified as k. The ratio of initial $\frac{\sigma}{\mu}$ was used to compare the calculated grain growth constant from this real microstructure to the model results from Baskaran's original work, Fig. 12. A 3.9 % relative increase in the grain growth constant compared to the homogeneous case was observed in the real microstructure that had $\frac{\sigma}{\mu} = 1.78$. This is consistent with the closest model structure with $\frac{\sigma}{\mu} = 1.75$ and a relative increase of 5.1 % in grain growth constant. This result shows that the increase in grain growth constant cannot be attributed to the artificial connectivity of the subdomains in Baskaran's model microstructures.

The real microstructure had a relatively modest $\frac{\sigma}{\mu}$ compared to the extreme model cases that showed larger deviations in k from k_0. While the 2D simulations suggest that the gradient in grain size has an effect on early stage grain growth, this has yet to be confirmed in 3D simulations or in experiments. Experimentally testing this grain growth anomaly requires samples with wider ranges of grain size and larger gradients in grain size. As the grain boundary properties were isotropic in the model and special boundaries were not considered, experiments on alloys should target materials with high stacking fault energies, *i.e.* those without annealing twins. The method described in this paper could be used to produce such samples for future work.

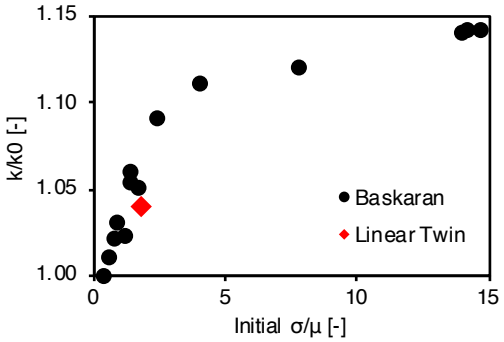

Fig. 12: Parabolic grain growth constant determined from gradient grain size microstructures with various ratios of the standard deviation to the mean (σ/μ) of the sample grain size distribution at initial time. The grain growth constant is normalized to a reference value from a spatially homogeneous grain size distribution. The black points are data from model gradient microstructures after [17] and the red diamond corresponds to an initial microstructure generated from the centroids of the linear twin sample corresponding to Fig. 11.

3.4 Recommendations

While 800H is a workhorse alloy for some applications and the performance of 800H pigtails was the motivation for this study, it was not the best alloy choice for a study of gradient grain size distributions due to lack of supporting information. Recrystallization of alloy 800H after cold work has not been widely studied in the literature. Further, minor nitride and carbide phases with solvi in the annealing temperature range of interest may complicate matters [30]. A more widely understood single-phase alloy with well known thermo-mechanical relations, for example alpha brass or pure nickel, would be a better choice.

The laser etched grid used here for strain measurement carried large uncertainties and yielded data on a coarse grid. Digital image correlation would be a much better choice for better spatial resolution of non-uniform strains on tensile samples [53].

In this work, we demonstrate an expedient method of generating grain size gradients in non-uniform tensile samples. Future work will include exploring the limits of this method in order to create larger differences in mean grain size between regions and also creating larger spatial gradients in the mean grain size between regions. These can be accomplished by decreasing the grain size in the smallest

grained regions and increasing the grain size in the large grained region. The first can be accomplished by increasing the maximum stored cold work and by annealing until the completion of recrystallization. Grain growth tends to decrease the grain size gradient as the mean grain size in the smallest grained region increases faster than the mean grain size in the large grained region. The grain size in the large grained region can be increased by ensuring that the cold work exceeds any critical strain for recrystallization.

The performance of alloys in industrial applications where gradients in grain size exist in actual components can be studied systematically. Production of gradient grain size samples using our method will enable laboratory experiments under controlled conditions with realistic microstructures. Future work includes investigating creep in gradient grain size microstructures of alloy 800H to understand the role of the gradient in failure of reformer pigtails.

The most interesting possibility is to use gradient grain size samples as a platform for parallel experiments on phenomena that depend on grain size. Appropriately designed samples where different regions have different grain sizes could be used to study important processes such as fatigue, environmentally assisted cracking, corrosion, precipitation, recrystallization, bulk phase changes, complexion transitions at grain boundaries, electrical properties and mass transport properties. Because the microstructures change continuously in our samples, determining metrics for regions that are microstructurally independent of each other is a future challenge.

High-throughput screening of microstructures has been identified by Miracle and Senkov [54] as an unmet challenge for the development of high entropy alloys. This class of alloys is vast, and without high-throughput computational and experimental techniques, the time to discover new, useful chemistries will be prohibitive. Our method could be used to focus co-optimization of alloy composition and microstructure to narrow the search space for new high entropy alloys.

High-throughput screening with gradient microstructure samples would accelerate the process of qualifying novel materials for applications such as biomedical or nuclear that have lengthy or involved qualification processes. For example, new alloys are sought for molten salt reactors [55] where the ASME Boiler and Pressure Vessel Code requires 100 000 hour creep rupture tests [56] in addition to a battery of other tests.

4 Conclusions

A general method to create alloy samples with two different designed gradients in grain size was demonstrated using Incoloy 800H. Non-uniform cold work and subsequent recrystallization annealing yielded two samples with mesoscopic gradients in grain size. Using the outlier grain method from ASTM Standard E1181 [23], both microstructures were characterized as topological duplex microstructures with $\Delta n > 3$. The spatial variation in grain size distribution was analyzed by sorting grains into 4 mm bins based on the centroids. The grain size gradients were $0.0081\,\mathrm{mm}^2/\mathrm{mm}$ and $0.0112\,\mathrm{mm}^2/\mathrm{mm}$ over 14 mm in the linear and sinusoidal samples, respectively. The grain size in the small grained region is likely to be overestimated due to EBSD step size limits. The grain size in the large grain region is likely to be underestimated due to sample truncation of the largest grains.

Grain size was a decreasing function of the measured plastic deformation. All regions had grain sizes exceeding the as-received material's, which indicates that grain growth had occurred over all regions of the samples. No evidence for the critical strain anneal was observed for static recrystallization of 800H during annealing at 1100 °C for 60 min.

No clear stress concentrations in the gradient grain size region were identified in preliminary finite element simulations using OOF2 [48] on the raw sinusoidal EBSD orientation map. No correlation between creep damage and microstructure could be drawn from this 2D calculation.

The parabolic grain growth constant $\frac{k}{k_0} = 1.039$ from a 2D simulation using the twin volumes in the linear sample with $\frac{\sigma}{\mu} = 1.78$ was consistent with the increase observed by Baskaran *et al.* [17] in model microstructures. This result is not explained by current grain growth theories. Grain growth experiments on gradient microstructures like those demonstrated here are necessary to test the predictions.

The method outlined in this paper demonstrates a simple method to design and thermomechanically process alloys to obtain intentional gradients in grain size. Such samples may provide insight into the relation between creep in Incoloy 800H pigtails and the microstructure for direct industrial application [16]. They can be used to test the grain growth predictions from Baskaran [17].

Further, these gradient grain size samples could be used for parallel experiments on a single specimen to develop understanding of phenomena that are affected by grain size such as complexion transitions at grain boundaries, transport properties and bulk phase transformations.

Most importantly, gradient samples could be used for high-throughput, parallel testing of microstructures. High-throughput testing methods are especially sought after for high entropy alloy development [54], where the compositional space is dauntingly large, and for new nuclear alloys [56], where the qualification process requires lengthy tests.

Acknowledgements CMB acknowledges A. D. Rollett for fruitful discussions on the statistical analysis and J. W. Bishop for suggesting methods for the spatial analysis. The authors thank A. Baskaran for performing the grain growth simulation. The authors thank P. Tait of Methanex for supporting this research.

Conflict of interest

The authors declare that they have no conflicts of interest.

5 References

References

1. W. D. Callister Jr, D. G. Rethwisch: Materials Science and Engineering: An Introduction: 9th Edition: John Wiley & Sons, Hoboken, NJ, 2014.
2. V. Cannillo, L. Lusvarghi, T. Manfredini, M. Montorsi, C. Siligardi, A. Sola: Journal of the European Ceramic Society Jan. 2007, vol. 27 (2), pp. 1293–1298.
3. A. Mortensen, S. Suresh: International Materials Reviews Jan. 1995, vol. 40 (6), pp. 239–265.
4. S. Suresh, A. Mortensen: International Materials Reviews Jan. 1997, vol. 42 (3), pp. 85–116.
5. A. R. Damodaran, S. Pandya, Y. Qi, S.-L. Hsu, S. Liu, C. Nelson, A. Dasgupta, P. Ercius, C. Ophus, L. R. Dedon, J. C. Agar, H. Lu, J. Zhang, A. M. Minor, A. M. Rappe, L. W. Martin: Nature Communications May 2017, vol. 8, pp. 14961.
6. J. V. Mantese, A. L. Micheli, N. W. Schubring, R. W. Hayes, G. Srinivasan, S. P. Alpay: Applied Physics Letters Aug. 2005, vol. 87 (8), pp. 082503.
7. J. Dossett (Ed.): Steel Heat Treating Fundamentals and Processes: Vol. 4A of ASM Handbook: ASM International, Materials Park, OH, 2014.

8. J. K. Lee, F. R. Ehrlich, L. A. Crall, T. H. Collins: Metallurgical Transactions A Feb. 1988, vol. 19 (2), pp. 329–335.
9. K.-H. Hwang, M. R. Plichta, J. K. Lee: Materials Science and Engineering: A May 1988, vol. 101, pp. 183–192.
10. K.-H. Hwang, M. R. Plichta, J. K. Lee: Materials Science and Engineering: A Jul. 1989, vol. 114, pp. 61–71.
11. J. Yan, J. Ma, J. Wang, Y. Shen: Metallurgical and Materials Transactions A Nov. 2018, vol. 49 (11), pp. 5333–5338.
12. J. Long, Q. Pan, N. Tao, M. Dao, S. Suresh, L. Lu: Acta Materialia Dec. 2018, .
13. Z. Cheng, H. Zhou, Q. Lu, H. Gao, L. Lu: Science Nov. 2018, vol. 362 (6414), pp. eaau1925.
14. P. Kodali, J. P. Richert: Failure Mechanisms of Alloy 800H in Steam Reformer Furnace Pigtails: in: CORROSION 2003: NACE International, 2003.
15. ASME: Boiler and Pressure Vessel Code: Tech. Rep. Section VIII Division I: American Society of Mechanical Engineers: New York, NY, UNITED STATES 2007,.
16. H. Almostaneer, H. Schrijen, K. Barai, A. Al-Meshari: Advances in Materials and Processing Technologies Apr. 2015, vol. 1 (1-2), pp. 56–66.
17. A. Baskaran, D. Crist, D. Lewis: Modelling and Simulation in Materials Science and Engineering Sep. 2017, vol. 25 (6), pp. 065010.
18. K. Brakke: Surface Evolver Manual: Susquehanna University 2013,.
19. E04 Committee: ASTM E112-13: Test Methods for Determining Average Grain Size: Tech. rep.: ASTM International: West Conshohocken, PA 2013,.
20. E04 Committee: ASTM E1382 - 97(2015): Test Methods for Determining Average Grain Size Using Semiautomatic and Automatic Image Analysis: Tech. rep.: ASTM International: West Conshohocken, PA 2015,.
21. E04 Committee: ASTM E2627 - 13: Practice for Determining Average Grain Size Using Electron Backscatter Diffraction (EBSD) in Fully Recrystallized Polycrystalline Materials: Tech. rep.: ASTM International: West Conshohocken, PA 2013,.
22. E. Committee: ASTM E930 - Standard Test Methods for Estimating the Largest Grain Observed in a Metallographic Section (ALA Grain Size) - Engineering Workbench: Tech. rep.: ASTM International: West Conshohocken, PA 2018,.
23. E. Committee: ASTM E1181 - Standard Test Methods for Characterizing Duplex Grain Sizes - Engineering Workbench: Tech. rep.: ASTM International: West Conshohocken, PA 2015,.
24. Incoloy alloy 800H & 800HT: Tech. Rep. SMC-047: Special Metals Corporation: New Hartford, NY 2004,.
25. W. Ren, R. Swindeman: A Review of Alloy 800H for Applications in the Gen IV Nuclear Energy Systems: in: ASME 2010 Pressure Vessels and Piping Division/K-PVP Conference: American Society of Mechanical Engineers, 2010: pp. 821–836.
26. S. Watanabe, T. Shibasaki, T. Hokamura: Remaining Life Estimation of Alloy 800H Pigtail Material During High Temperature Service: in: CORROSION 2018: NACE International, 2018.
27. D. Drabble, C. Bishop, M. Kral: Metallurgical and Materials Transactions A: Physical Metallurgy and Materials Science 2011, vol. 42 (3), pp. 763–772.
28. L. Tan, L. Rakotojaona, T. R. Allen, R. K. Nanstad, J. T. Busby: Materials Science and Engineering: A Mar. 2011, vol. 528 (6), pp. 2755–2761.
29. E. Brünger, X. Wang, G. Gottstein: Scripta Materialia May 1998, vol. 38 (12), pp. 1843–1849.

30. Y. Cao, H. Di, J. Zhang, J. Zhang, T. Ma, R. D. K. Misra: Materials Science and Engineering: A Nov. 2013, vol. 585, pp. 71–85.
31. Y. Cao, H. Di, G. Huang: Journal of Nuclear Materials Apr. 2017, vol. 486, pp. 21–25.
32. W. S. Chen, W. Kai, L. W. Tsay, J. J. Kai: Nuclear Engineering and Design Jun. 2014, vol. 272, pp. 92–98.
33. A. L. Beardsley, C. M. Bishop, M. V. Kral: Metallurgical and Materials Transactions A Sep. 2019, vol. 50 (9), pp. 4098–4110.
34. A. Beardsley, C. Bishop, M. Kral: Materials Performance and Characterization 2016, vol. 5 (5), pp. 717–739.
35. Y. Cao, X. Shen, H. Di, G. Huang: Journal of Alloys and Compounds Mar. 2017, vol. 698, pp. 304–316.
36. C. A. Schneider, W. S. Rasband, K. W. Eliceiri: Nature Methods Jun. 2012, vol. 9, pp. 671–675.
37. MATLAB: Mathworks 2015,.
38. G. Palumbo, K. T. Aust, E. M. Lehockey, U. Erb, P. Lin: Scripta Materialia May 1998, vol. 38 (11), pp. 1685–1690.
39. V. Randle: Acta Materialia Aug. 2004, vol. 52 (14), pp. 4067–4081.
40. G. F. Vander Voort, J. J. Friel: Materials Characterization Dec. 1992, vol. 29 (4), pp. 293–312.
41. N. F. Hurley: AAPG Bulletin 1994, vol. 78 (8), pp. 1173–1185.
42. S. Wang, E. A. Holm, J. Suni, M. H. Alvi, P. N. Kalu, A. D. Rollett: Acta Materialia Jun. 2011, vol. 59 (10), pp. 3872–3882.
43. L. Chen, J. Chen, R. A. Lebensohn, Y. Z. Ji, T. W. Heo, S. Bhattacharyya, K. Chang, S. Mathaudhu, Z. K. Liu, L. Q. Chen: Computer Methods in Applied Mechanics and Engineering Mar. 2015, vol. 285, pp. 829–848.
44. T. Takaki, Y. Tomita: International Journal of Mechanical Sciences Feb. 2010, vol. 52 (2), pp. 320–328.
45. H. S. Zurob, Y. Bréchet, J. Dunlop: Acta Materialia Sep. 2006, vol. 54 (15), pp. 3983–3990.
46. J. E. Hatch: Aluminum: Properties and Physical Metallurgy: subsequent edition Edition: ASM International, Metals Park, Ohio, 1984.
47. M. E. Kassner: Fundamentals of Creep in Metals and Alloys: 3rd Edition: Butterworth-Heinemann, Waltham, MA, 2015.
48. A. C. E. Reid, R. C. Lua, R. E. Garcia, V. R. Coffman, S. A. Langer: International Journal of Materials and Product Technology May 2009, .
49. M. C. Mangalick, N. F. Fiore: Trans Met Soc AIME 1968, vol. 242 (11).
50. M. E. Kassner, T. A. Hayes: International Journal of Plasticity Oct. 2003, vol. 19 (10), pp. 1715–1748.
51. M. P. Petkov, J. Hu, E. Tarleton, A. C. F. Cocks: International Journal of Solids and Structures Oct. 2019, vol. 171, pp. 54–80.
52. G. Venkataramani, D. Deka, S. Ghosh: Journal of Engineering Materials and Technology Feb. 2006, vol. 128 (3), pp. 356–365.
53. V. Herrera-Solaz, L. Patriarca, S. Foletti, J. Segurado, M. Niffenegger: Materials Science and Engineering: A Mar. 2019, vol. 751, pp. 99–106.
54. D. B. Miracle, O. N. Senkov: Acta Materialia Jan. 2017, vol. 122, pp. 448–511.
55. O. Muránsky, C. Yang, H. Zhu, I. Karatchevtseva, P. Sláma, Z. Nový, L. Edwards: Corrosion Science Oct. 2019, vol. 159, pp. 108087.

521 56. R. Wright, T.-L. Sham: Status of Metallic Structural Materials for Molten Salt Reactors: Tech. Rep. INL/EXT-18-
522 45171: United States Department of Energy: Idaho National Laboratory May 2018,.

6 Tables

Table 1: Properties for FEA sample design of 800H

Property	Value	Source
Density	$7940\,\mathrm{kg\,m^{-3}}$	[24]
Elastic modulus	196.5 GPa	[24]
Poisson ratio	0.339	[24]
Yield strength	250 MPa	This work
Tangent modulus	1.8 GPa	This work

Table 2: Geometry and tensile test parameters determined by FEA. w_{min} is the minimum gage width. $w(x)$ is the shape of the gage width as a function of x in mm. ΔX_{max} is maximum cross head displacement. F_{max} is the maximum load.

	Linear	Sinusoidal
L	75 mm	75 mm
h	4.76 mm	4.76 mm
w_{min}	12 mm	12 mm
$w(x)$	$\frac{150}{x}$	$\frac{5}{\sin(\frac{\pi}{100}x)}$
ΔX_{max}	3 mm	4 mm
F_{max}	26.1 kN	23.7 kN

Table 3: Summary of grain size distribution statistics binned according to Fig. 7a) for the linear sample where N is the zeroeth moment or number of measurements, μ is the first moment or mean of the distribution and σ^2 is the second central moment or variance of the distribution.

Bin	2 mm	6 mm	10 mm	14 mm	18 mm	22 mm	26 mm	30 mm	34 mm	38 mm
$N[-]$	237	535	538	441	344	240	183	130	105	96
$\mu[\mathrm{mm}^2]$	0.0413	0.0362	0.0358	0.0445	0.0572	0.0781	0.1112	0.1415	0.1860	0.1851
$\sigma^2[\mathrm{mm}^4]$	0.0088	0.0025	0.0024	0.0041	0.0083	0.0092	0.0372	0.0383	0.0516	0.0542

Table 4: Summary of grain size distribution statistics binned according to Fig. 7b) for the sinusoidal sample where N is the zeroeth moment or number of measurements, μ is the first moment or mean of the distribution and σ^2 is the second central moment or variance of the distribution.

Bin	2 mm	6 mm	10 mm	14 mm	18 mm	22 mm	26 mm	30 mm	34 mm	38 mm
$N[-]$	254	449	428	391	338	247	181	128	83	70
$\mu[\text{mm}^2]$	0.0374	0.0415	0.0438	0.0487	0.0554	0.0767	0.1056	0.1434	0.2343	0.2329
$\sigma^2[\text{mm}^4]$	0.0032	0.0027	0.0043	0.0076	0.0134	0.0108	0.0239	0.0551	0.1044	0.1816

Table 5: Summary of twin grain size distribution statistics binned according to Fig. 11 for the linear sample where N is the zeroeth moment or number of measurements, μ is the first moment or mean of the distribution and σ^2 is the second central moment or variance of the distribution.

Bin	2 mm	6 mm	10 mm	14 mm	18 mm	22 mm	26 mm	30 mm	34 mm	38 mm
$N[-]$	880	2105	2188	2034	1740	1406	1122	874	752	664
$\mu[\text{mm}^2]$	0.0111	0.0092	0.0089	0.0096	0.0111	0.0138	0.0172	0.0222	0.0259	0.0263
$\sigma^2[\text{mm}^4]$	0.0005	0.0002	0.0002	0.0002	0.0003	0.0004	0.0008	0.0010	0.0019	0.0017